Early-arrival waveform inversion by one-way wavefield extrapolation

Jeff Shragge

Stanford Exploration Project, Mitchell Bldg., Department of Geophysics,

Stanford University, Stanford, CA 94305-2215

(January 10, 2007)

ABSTRACT

One-way Riemannian wavefield extrapolation (RWE) on computational meshes conforming to the direction of turning-wave propagation is presented as an alternative forward modeling procedure for waveform inversion. Forward modeling tests demonstrate that the RWE approach accurately calculates the early-arrival wavefield phases important for waveform inversion. Initial results indicate that RWE waveforms are well matched at wide offsets to finite-difference data, and can be used in a waveform inversion scheme to invert synthetic data for moderate 1D velocity perturbations.

INTRODUCTION

Frequency-domain waveform inversion has been successfully demonstrated in numerous 2D applications (Pratt and Worthington, 1989; Crase et al., 1990; Pratt and Shipp, 1999; Dessa et al., 2004); however, few 3D examples have yet to be reported. The predominant reason is that using finite-differences (FD) as the forward modeling operator typically results in a large, but relatively sparse, impedance matrix that is usually inverted via LU decomposition. A limitation of this approach - especially when considering any 3D extensions - is the memory required for performing matrix inversion.

For 2D inversion problems, the memory requirement for an LU decomposition using graph theoretic techniques that exploit matrix sparsity is roughly n^3, where n is the average model space dimension (Štekl and Pratt, 1998). The memory requirement for typical 3D exploration blocks, though, rises to nearly $n^{4.6}$ (Operto et al., 2006), which currently is impractical for routine exploration implementation.

An alternative to finite differencing is to employ a forward modeling scheme based on one-way wavefield extrapolation. Although less accurate than FD owing to the physical approximations made when deriving one-way wave-equations, the corresponding extrapolation operators can still be used to calculate phases (and perhaps the amplitudes) of the early arrivals commonly used in waveform inversion. This paper examines the idea of performing wavefield extrapolation on meshes oriented in the general direction of turning-wave propagation. By incorporating the bulk orientation directly into the coordinate system, lower-order Riemannian wavefield extrapolation operators (Sava and Fomel, 2005) can be used to calculate the early arrivals of wide-offset seismic data. Importantly, 3D forward modeling by wavefield extrapolation involves manageable memory requirements, leaving computational complexity as the main computational constraint (approximately $n^3(\log_2 n)^2 ns$, where ns is number of sources (Biondi, 2006)). Thus, one-way wavefield extrapolation potentially offers computational and memory savings and is worth examining in the context of waveform inversion.

FREQUENCY-DOMAIN WAVEFORM INVERSION

Prescribing a forward modeling operator is the initial step in any frequency-domain waveform inversion procedure. (The reader wishing to have a more complete overview is referred to Pratt (1998), Sirgue and Pratt (2004) and references therein.) Assuming that wave propagation is adequately governed by an acoustic wave equation, the forward-modeling procedure generates a scalar wavefield that

is a solution to the Helmholtz equation. The data residuals, or the difference between the observed and modeled data, are then used to generate velocity model updates. This is commonly accomplished by iteratively minimizing the l_2 residual misfit at each successive frequency through computing the negative gradient with respect to the variation in model parameters (Pratt and Worthington, 1989).

Methods for calculating the gradient without explicitly computing the partial derivatives of the data are well established (Lailly, 1983; Tarantola, 1984; Pratt et al., 1998). The main time-domain result is that the gradient vector can be computed in a computational domain, $\mathbf{x}$, by zero-lag correlation of the wavefield propagated causally from source point, $\mathbf{s}$, and the data residuals propagated acausally from receiver location, $\mathbf{r}$. In the frequency domain (ω), this involves multiplying two monochromatic wavefields: an assumed unit amplitude and zero-phase source Green's function, $G_0(\mathbf{s},\mathbf{x};\omega)$; and a residual wavefield comprised of a collection of receiver Green's functions, $G_0(\mathbf{x},\mathbf{r};\omega)$, individually weighted by the data residual value, $\Delta\Psi(\mathbf{s},\mathbf{r};\omega)$. This leads to the following expression for gradient vector, $g(\mathbf{x})$,

$$g(\mathbf{x};\omega) = -\omega^2 \sum_{\mathbf{s}} \sum_{\mathbf{r}} \Re\left[G_0^*(\mathbf{s},\mathbf{x};\omega) G_0^*(\mathbf{x},\mathbf{r};\omega) \Delta\Psi(\mathbf{s},\mathbf{r};\omega)\right], \tag{1}$$

where $\Re$ indicates the real component, and * represents complex conjugate (Sirgue and Pratt, 2004). The summation over sources and receivers is done for each non-linear iteration at each frequency. The bracketed expression representing the back-projected data residuals may be regarded as a "migration of the residual wavefield data" (Mora, 1987). Thus, a central component of a practical waveform inversion implementation, like in any seismic migration analysis, is an accurate and efficient calculation of the source and receiver Green's functions, $G_0(\mathbf{s},\mathbf{x};\omega)$ and $G_0(\mathbf{x},\mathbf{r};\omega)$. The optimal trade-off between these two competing constraints, especially for 3D implementations, remains an open question that merits further investigation.

AN ALTERNATE FORWARD MODELING APPROACH

An alternate strategy for computing Green's functions for waveform inversion is to consider one-way propagation on coordinate systems designed especially for calculating wide-offset, early-arrival wavefields. One interesting example is a sideways-tilted, ray-like mesh with an extrapolation axis oriented predominately in the direction of turning-wave propagation (see upper left panel of figure 1). In this reference frame, the bulk of wavefield propagation occurs at low angles to the extrapolation axis where the phases and amplitudes calculated by one-way operators remain fairly accurate. One-way propagation in generalized coordinates is described by Riemannian wavefield extrapolation, which encodes the mesh geometry directly into the extrapolation operator using additional mixed-domain coefficients. (The reader interested in additional information on RWE is referred to Sava and Fomel (2005) and Shragge (2007).)

The utility of the RWE forward-modeling approach is illustrated in figure 1, which shows wavefield propagation in both the Cartesian (left panels) and the "turning-wave" coordinate domains (right panels). The upper left panel shows a turning-wave mesh overlying part of the SMAART JV Pluto 1.5 P-wave velocity model. The upper right panel depicts this velocity model interpolated to a transform RWE domain parameterized by 'shooting angle' and 'extrapolation step' axes. The source wavefield, $G_0(\mathbf{s},\mathbf{x};\omega)$, is generated by propagating an initially planar wavefield (as a function of shooting-angle) through each successive extrapolation step. Modeled data are generated by extracting the wavefield values at the streamer depth. The lower right and left panels show the same four superimposed wavefield snapshots (at 1.0 s, 2.2 s, 3.4 s and 4.6 s) in the RWE and Cartesian domains, respectively. Note that while some wavefield energy is not modeled - e.g. near-vertical wavepaths - the bulk of the direct wavefield energy propagates throughout the model at low angles to the extrapolation axis. Numerous reflected phases, including those from the top-salt, are evident in the lower panels. These reflections

are not "true-amplitude", though, because there is no formal accounting for reflection coefficients.

One-way extrapolation results for the Pluto model using the turning-wave coordinate mesh shown in figure 1 are presented in the right panel of figure 2. The corresponding finite-difference data are shown in the left panel. Although the reflections evident in the near-offset traces of the FD data are completely absent from the RWE data, the wavefields at wider offsets become increasingly similar. This observation should not be surprising: the coordinate mesh was designed specifically to calculate the wide-offset early arrivals important for the initial stages of waveform inversion. Figure 3 presents waveform comparisons at four wide offsets. The FD and RWE modeled waveforms were low-pass filtered to a frequency band typically used for exploration-scale waveform inversion. Note that the early arrivals of two sets of waveforms are well-matched in phase, though less so in amplitude.

Back-projecting wavefield residuals to form the gradient vector is accomplished with a waveform injection approach that is the adjoint operation of wavefield data extraction. The residual wavefield, initially limited to the data residual from the farthest receiver, is propagated back towards the source point. As each successive receiver is reached, the data residual at that point is injected into the residual wavefield and extrapolated to the next step. Gradient vector $g(\mathbf{x})$ is then calculated by multiplying the residual and the stored source wavefields at each step and interpolating the result back to the Cartesian domain.

Figure 4 presents a gradient vector example for an offset source-receiver pair centered in mirrored half-space velocity model (upper left panel). The upper right panel shows a monochromatic wavefield propagated outward from the source point, $G_0(\mathbf{s},\mathbf{x};\omega)$, while the lower right panel shows the residual wavefield back-propagated from the single receiver, $G_0(\mathbf{x},\mathbf{r};\omega)$. Multiplying these two wavefields generates the "wavepath" (Woodward, 1992) in the lower left panel that is central to the waveform inversion approach.

1D WAVEFORM INVERSION TEST

Figure 5 presents the results of a 1D waveform inversion test using one-way Riemannian wavefield extrapolation as the forward modeling operator. The waveform inversion goal is to reconstruct the $+10\%$ velocity perturbation shown in the right panel using the approach described in Sirgue and Pratt (2004) assuming a constant 2 kms^{-1} starting velocity model. The FD data in the left panel consist of a linear direct arrival and two hyperbolic reflection events of opposing sign from the top and bottom of the velocity perturbation. The synthetic data were low-pass filtered, windowed to eliminate boundary artifacts, and zeroed at locations <2 km from the source point. The frequencies selected for inversion were between 3-12 Hz at 0.25 Hz intervals.

Waveform inversion results after five non-linear iterations at each frequency are shown in the right panel of figure 5. The recovered velocity profile perturbation is almost correctly centered, but contains significant negative side lobes both above and below the true perturbation depths. This result is similar to the 1D experiment of Sirgue and Pratt (2004), who demonstrate that the inverted velocity profiles do not contain all necessary - and especially the lower - spatial frequency components. These are likely recoverable if the inversion were to include lower (temporal) frequency data and offsets sufficiently wide to generate significant "image-stretch" phenomena.

CONCLUDING REMARKS

This paper describes an alternate forward modeling approach for frequency-domain waveform inversion based on one-way wavefield extrapolation. The results suggest that the phases (and perhaps amplitudes) of forward modeled data are sufficiently accurate for use in early-arrival waveform inversion analysis. Importantly, 3D wavefield extrapolation is now routine in practice, suggesting that upscaling this approach to 3D waveform inversion would not be too computationally restrictive. In

addition, amplitude accuracy would likely be improved by incorporating the factor described by Zhang et al. (2003) into the RWE extrapolation operators. Alternatively, one could consider using the "true-amplitude" one-way extrapolation operators of Thomson (2005) that provide a more formal accounting of reflection coefficients and transmission losses.

ACKNOWLEDGMENTS

I thank Drew Brenders, Colin Thomson, and Clement Kostov for helpful discussions and acknowledge Schlumberger Cambridge Research for their support during a summer internship where this research was carried out. The sponsors of the Stanford Exploration Project are also acknowledged for their continuing financial support.

REFERENCES

Biondi, B., 2006, 3-D Seismic Imaging: Society of Exploration Geophysicists.

Crase, E., A. Pica, et al., 1990, Robust elastic nonlinear waveform inversion: Application to real data: Geophysics, **55**, 527–538.

Dessa, J.-X., S. Operto, et al., 2004, Multiscale seismic imaing of the eastern Nankai trough by full waveform inversion: Geophysical Research Letters, **31**, doi:10,1029/2004GL020453.

Lailly, P., 1983, The seismic inverse problem as a sequence of pre-stack migration: Society of Industrial and Applied Mathematics, Bednar, J.B., Redner, R., Robinson, E. and Weglein, A., Eds., Conference on inverse scattering: Theory and Applications.

Mora, P., 1987, Nonlinear two-dimensional elastic inversion of multioffset seismic data: Geophysics, **52**, 1211–1228.

Operto, S., J. Virieux, et al., 2006, 3D frequency-domain finite-difference modeling of acoustic waves using massively parallel direct solver: A feasibility study: 75^{th} SEG Ann. Gen. MeetingConference and Exhibition, Expanded Abstracts.

Pratt, R. and R. Shipp, 1999, Seismic waveform inversion in the frequency domain, Part 2: Fault delineation in sediments using crosshole data: Geophysics, **64**, 902–914.

Pratt, R. and M. Worthington, 1989, The application of diffraction tomography to cross-hole seismic data: Geophysics, **53**, 1284–1294.

Pratt, R., C. Shin, and G. Hicks, 1998, Gauss-Newton and full Newton methods in frequency space seismic waveform inversion: Geophysical Journal International, **133**, 323–340.

Pratt, R., 1998, Seismic waveform inversion in the frequency domain, Part 1: Theory and verification in a physical scale model: Geophysics, **64**, 888–901.

Sava, P. and S. Fomel, 2005, Riemannian wavefield extrapolation: Geophysics, **70**, T45–T56.

Shragge, J., 2007, Riemannian wavefield extrapolation: Non-orthogonal coordinate systems: submitted to Geophysics, **xx**, xxx–xxx.

Sirgue, L. and R. Pratt, 2004, Efficient waveform inversion and imaging: A strategy for selecting temporal frequencies: Geophysics, **69**, 231–248.

Tarantola, A., 1984, Linearized inversion of seismic reflection data in the acoustic approximation: Geophysics, **49**, 998–1015.

Thomson, C., 2005, Accuracy and efficiency considerations for wide-angle wavefield extrapolators and scattering operators: Geophys. J. Int., **163**, 308–323.

Štekl, I. and R. Pratt, 1998, Accurate visco-elastic modeling frequency-domain finite differences using rotated operators: Geophysics, **63**, 1779–1794.

Woodward, M., 1992, Wave-equation tomography: Geophysics, **57**, 15–26.

Zhang, Y., G. Zhang, and N. Bleistein, 2003, True amplitude wave equation migration arising from true amplitude one-way wave equations: Inverse Problems, **19**, 1113–1138.

LIST OF FIGURES

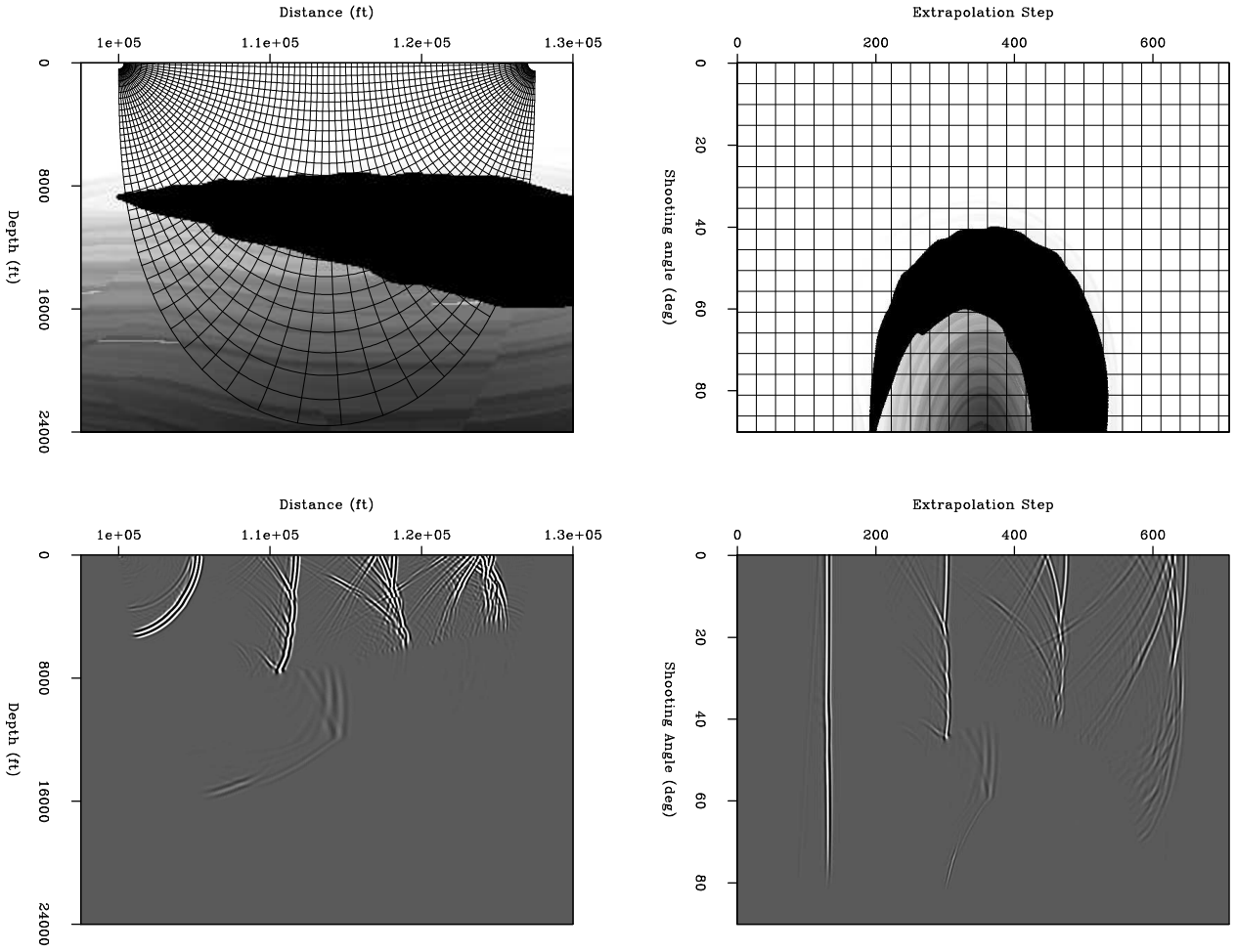
Distance (ft)
1e+05
1.1e+05
1.2e+05
1.3e+05
Depth (ft)
0
8000
16000
24000
Extrapolation Step
0
200
400
600
Shooting angle (deg)
0
20
40
60
80
Distance (ft)
1e+05
1.1e+05
1.2e+05
1.3e+05
Depth (ft)
0
8000
16000
24000
Extrapolation Step
0
200
400
600
Shooting Angle (deg)
0
20
40
60
80

Figure 1.

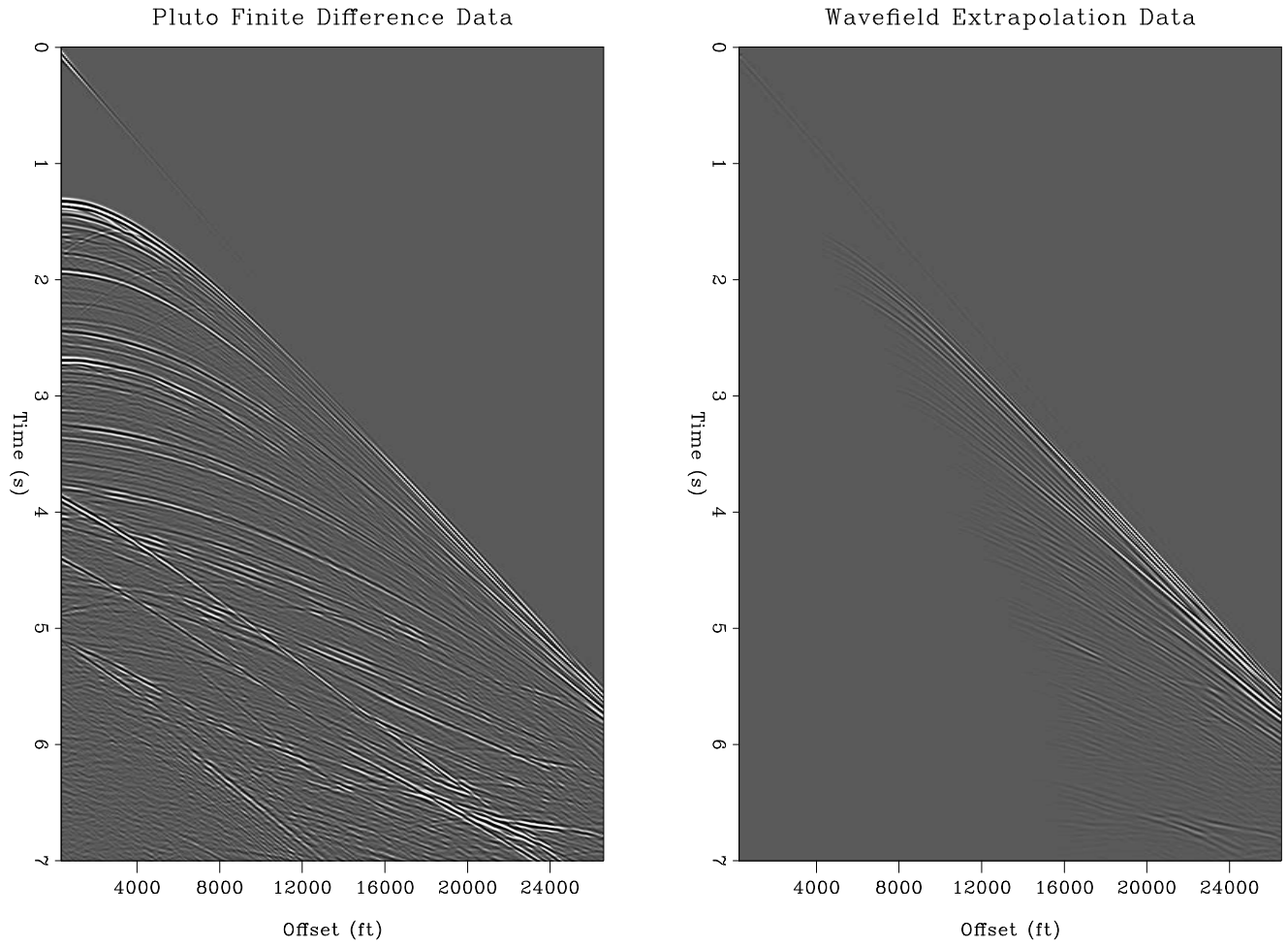
Pluto Finite Difference Data
Wavefield Extrapolation Data
Time (s)
Offset (ft)
0
1
2
3
4
5
6
7
4000
8000
12000
16000
20000
24000

Figure 2.

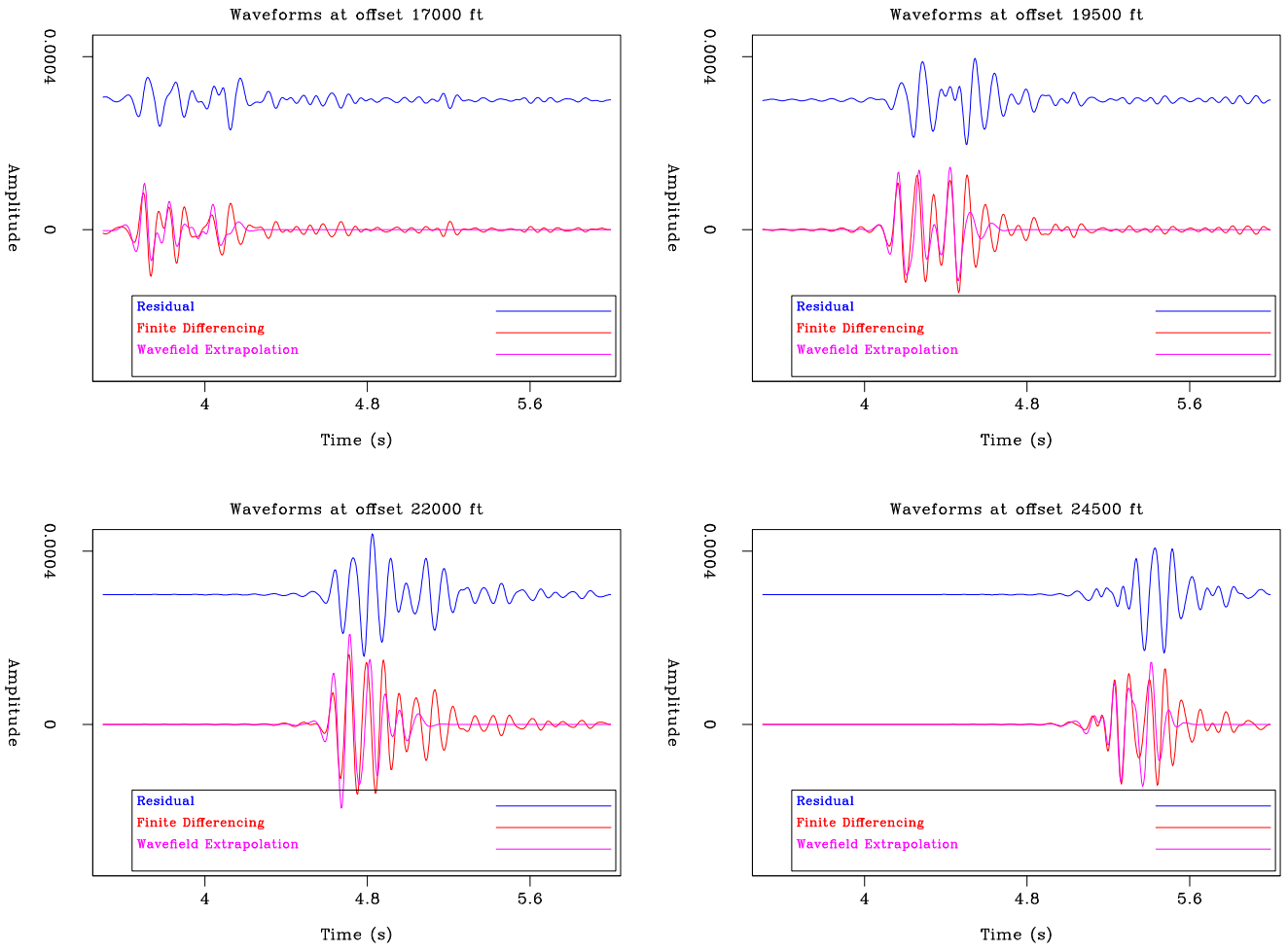
Waveforms at offset 17000 ft
Waveforms at offset 19500 ft
Waveforms at offset 22000 ft
Waveforms at offset 24500 ft
Amplitude
0.0004
0
4
4.8
5.6
Time (s)
Residual
Finite Differencing
Wavefield Extrapolation

Figure 3.

Velocity Model

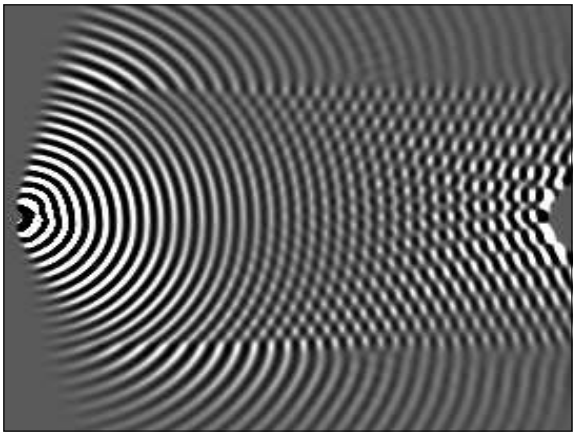

Forward−propagated wavefield

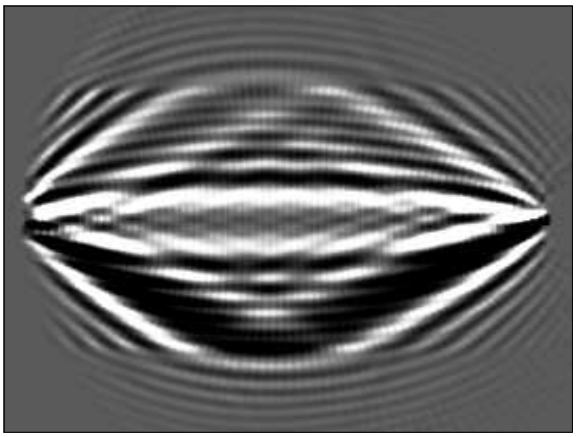

Wavepath

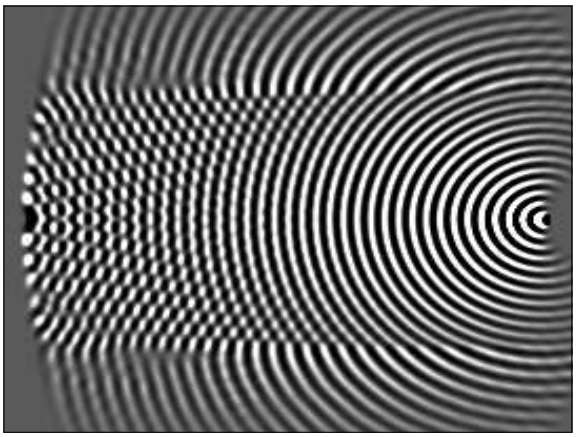

Back−propagated wavefield

Figure 4.

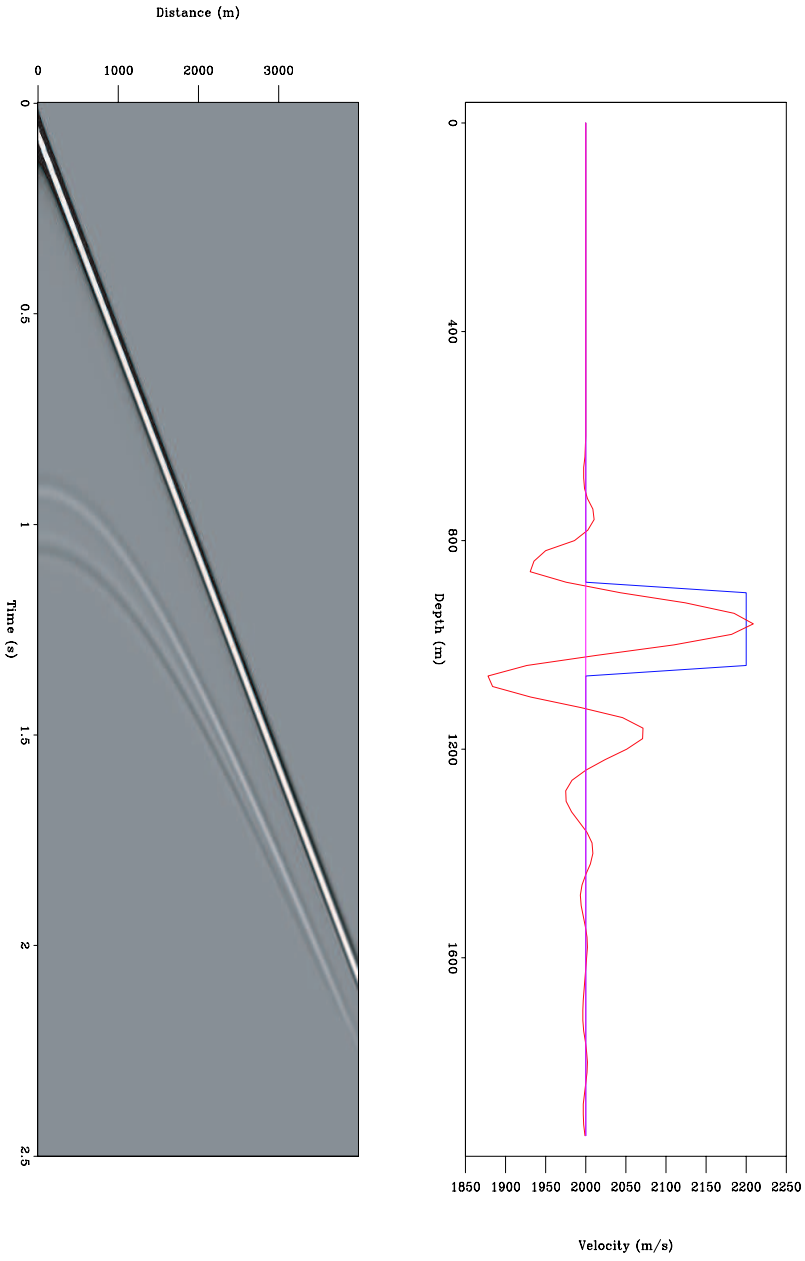
Distance (m)
0
1000
2000
3000
Time (s)
0
0.5
1
1.5
2
2.5
Depth (m)
0
400
800
1200
1600
1850
1900
1950
2000
2050
2100
2150
2200
2250
Velocity (m/s)

Figure 5.